

What a twist cell experiment tells about a quartic twist theory for chromonics

Silvia Paparini* and Epifanio G. Virga†

Department of Mathematics, University of Pavia, Via Ferrata 5, 27100 Pavia, Italy

(Dated: February 27, 2024)

The elastic theory of chromonic liquid crystals is not completely established. We know, for example, that for anomalously low twist constants (needed for chromonics) the classical Oseen-Frank theory may entail paradoxical consequences when applied to describe the equilibrium shapes of droplets surrounded by an isotropic phase: contrary to experimental evidence, they are predicted to dissolve in a plethora of unstable smaller droplets. We proposed a *quartic twist* theory that prevents such an instability from happening. Here, we apply this theory to the data of two experiments devised to measure the planar anchoring strength at the plates bounding a twist cell filled with a chromonic liquid crystal; these data had before been interpreted within the Oseen-Frank theory. We show that the quartic twist theory affords a better agreement with the experimental data, while delivering in one case a larger value for the anchoring strength.

I. INTRODUCTION

Chromonic liquid crystals are lyotropic phases, here abbreviated LCLCs, in which plank-shaped molecules arrange themselves in stacks when dissolved in solution (usually aqueous). For sufficiently large concentrations, the constituting stacks give rise to an ordered phase, either nematic or columnar [1–5].

Here, we shall only be concerned with the nematic phase. Numerous substances have a LCLC phase; these include organic dyes (especially those common in food industry), drugs, and oligonucleotides. Since LCLCs are mostly dispersed in water, they are also likely to have plenty of applications in life sciences [6–9].

As pointed out in [10], successful applications of LCLCs presume the ability to control the orientation of the director \mathbf{n} in their nematic phase, and this can only be done by characterizing the anchoring performance of diverse surface treatments. Planar anchoring of LCLCs on surfaces has been achieved by a number of methods, which include irradiation with polarized light of azo-polymer substrates [11–15], mechanical rubbing of polymer surface coatings [16, 17] as well as of bare glass [18, 19], and fabrication of closely spaced surface ridges [20, 21].

The alignment method adopted in [10], one of the experimental works that motivated our theoretical investigation, uses commercially available rubbed polyimide (PI) layers, known to induce a good planar alignment on solutions of disodium cromoglycate (DSCG), an anti-asthmatic drug.

When a nematic liquid crystal is placed in a cell between two parallel plates promoting planar (weak) anchoring along directions at right angles to one another, the nematic director \mathbf{n} acquires a twist distortion in the cell. If the anchoring strength W_0 is not infinite, however, \mathbf{n} at the plates departs by an *offset* angle δ from the preferred *easy* axis, so that the overall twist angle Ω is less than $\pi/2$. Clearly, the smaller is W_0 , the larger is δ .

Building on earlier work [19], the experiment performed in [10] determined W_0 at the plates bounding a cell filled with a DSCG aqueous solution by measuring optically Ω . The measured value of W_0 turned out to be less than $1 \mu\text{J}/\text{m}^2$. A larger value of W_0 was measured in [15], which adopted an experimental method similar to that used in [10], but with a different substrate.

The elastic theory employed in both [10] and [15] is the classical quadratic Oseen-Frank theory, with an anomalously small twist constant K_{22} . In particular, K_{22} must be smaller than the saddle-splay constant K_{24} , thus violating one of the inequalities Ericksen [22] had put forward to guarantee that the Oseen-Frank stored energy be bounded below. However, as shown in [23], free-boundary problems may reveal noxious consequences stemming from violating Ericksen's inequalities. If $K_{22} < K_{24}$, a LCLC droplet surrounded by an isotropic fluid environment (enforcing degenerate planar anchoring for the director at the interface) is predicted to be unstable against *shape* perturbations: it would split indefinitely in smaller droplets, while the total free energy plummets to negative infinity [23].

This prediction is in sharp contrast with the wealth of experimental observations of LCLC tactoidal¹ droplets in the biphasic region of phase space, where nematic and isotropic phases coexist in equilibrium [24–28]. These studies have consistently reported stable twisted bipolar tactoids.

To resolve this contradiction, in [29] we proposed a minimalist quartic theory for LCLCs, which adds to the Oseen-Frank energy density a single quartic term in the twist measure; hence the name *quartic twist* theory. We showed in

* silvia.paparini@unipv.it

† eg.virga@unipv.it

¹ *Tactoids* are elongated, cylindrically symmetric shapes with pointed ends as poles.

[29] that indeed within this theory the total free energy of chromonic droplets subject to degenerate planar interfacial anchoring remains bounded below, even if $K_{22} < K_{24}$.

In [30], the quartic twist theory was applied to explain the formation of *inversion rings* within spherical cavities enclosing water solutions of SSY (Sunset Yellow, a dye used in industrially processed food) subject to *homeotropic* boundary conditions for \mathbf{n} . The predictions of the theory were recently corroborated by some experimental evidence [31, 32].

Here, we reexamine the experiments performed in [10] and [15] in the light of the quartic twist theory. We show that this also predicts a *linear* twist between the cell's plates with an offset angle related to both the anchoring strength W_0 and a phenomenological length a featuring in the theory. The data presented in both [10] and [15] turn out to be better fitted by this theory compared to the classical quadratic one (with errors decreased by 3% and 1.4%, respectively); as a result, both W_0 and a are determined, the former with a value larger than that found in [10] and much closer to that found in [15].

The rest of the paper is organized as follows. In Section II, we summarize the quartic twist theory employed here, recalling only its essential features. In Section III, we apply this theory to a $\pi/2$ twist cell with weak planar anchoring and we employ it to reinterpret the experimental data of [10] and [15]. Finally, we summarize our conclusions in Section IV. The paper is closed by two appendices: one shows that the weak anchoring is never fully broken in the case under study, and the other gives details on the error estimates involved in data fitting.

II. QUARTIC TWIST THEORY

What makes chromonic nematics differ from ordinary ones is the *ground state* of their distortion: a *double* twist for the former, a uniform field (along any selected direction) for the latter. We now explore this difference in more detail.

We follow Selinger [33] in writing the elastic energy density of the Oseen-Frank theory in an equivalent form,

$$W_{\text{OF}}(\mathbf{n}, \nabla \mathbf{n}) = \frac{1}{2}(K_{11} - K_{24})S^2 + \frac{1}{2}(K_{22} - K_{24})T^2 + \frac{1}{2}K_{33}B^2 + 2K_{24}q^2, \quad (1)$$

where $S := \text{div } \mathbf{n}$ is the *splay*, $T := \mathbf{n} \cdot \text{curl } \mathbf{n}$ is the *twist*, $B^2 := \mathbf{b} \cdot \mathbf{b}$ is the square modulus of the *bend* vector $\mathbf{b} := \mathbf{n} \times \text{curl } \mathbf{n}$, and $q > 0$ is the *octupolar splay* [34] derived from the following equation

$$2q^2 = \text{tr}(\nabla \mathbf{n})^2 + \frac{1}{2}T^2 - \frac{1}{2}S^2. \quad (2)$$

Since (S, T, B, q) are independent *distortion measures*, it easily follows from (1) that W_{OF} is positive semi-definite whenever

$$K_{11} \geq K_{24} \geq 0, \quad (3a)$$

$$K_{22} \geq K_{24} \geq 0, \quad (3b)$$

$$K_{33} \geq 0, \quad (3c)$$

which are the celebrated *Ericksen's inequalities* [22]. If these inequalities are satisfied in strict form, the global ground state of W_{OF} is attained on the uniform director field, characterized by

$$S = T = B = q = 0, \quad (4)$$

which designates the ground state of ordinary nematics.

LCLCs are characterized by a different ground state, one where all distortion measures vanish, *but* T , which we call a *double twist*. Here, we adopt the terminology proposed by Selinger [35] (see also [36]) and distinguish between *single* and *double* twists. The former is characterized by

$$S = 0, \quad B = 0, \quad T = \pm 2q, \quad (5)$$

which designates a director distortion capable of filling *uniformly* the whole space [37].² Unlike this, a double twist *cannot* fill space uniformly: it can possibly be realized locally, but not everywhere. In words, we also say that it is a *frustrated* ground state.³ For the Oseen-Frank theory to accommodate such a ground state, inequality (3b) must be replaced by $K_{24} \geq K_{22} \geq 0$, but this comes at the price of making W_{OF} unbounded below [38].

² It is nothing but what others would call a *cholesteric* twist.

³ It was shown in [38] that a double twist can, for example, be attained exactly on the symmetry axis of cylinders enforcing degenerate planar anchoring on their lateral boundary.

The essential feature of the quartic twist theory proposed in [29] is to envision a double twist (with two equivalent chiral variants) as ground state of LCLCs in three-dimensional space,

$$S = 0, \quad T = \pm T_0, \quad B = 0, \quad q = 0. \quad (6)$$

The degeneracy of the ground double twist in (6) arises from the achiral nature of the molecular aggregates that constitute these materials, which is reflected in the lack of chirality of their condensed phases.

The elastic stored energy must equally penalize both ground chiral variants. Our minimalist proposal to achieve this goal was to add a *quartic twist* term to the Oseen-Frank stored-energy density,

$$W_{\text{QT}}(\mathbf{n}, \nabla \mathbf{n}) := \frac{1}{2}(K_{11} - K_{24})S^2 + \frac{1}{2}(K_{22} - K_{24})T^2 + \frac{1}{2}K_{23}B^2 + \frac{1}{2}K_{24}(2q)^2 + \frac{1}{4}K_{22}a^2T^4, \quad (7)$$

where a is a *characteristic length*. W_{QT} is bounded below whenever

$$K_{11} \geq K_{24} \geq 0, \quad (8a)$$

$$K_{24} \geq K_{22} \geq 0, \quad (8b)$$

$$K_{33} \geq 0. \quad (8c)$$

If these inequalities hold, as we shall assume here, then W_{QT} is minimum at the degenerate double twist (6) characterized by

$$T_0 := \frac{1}{a} \sqrt{\frac{K_{24} - K_{22}}{K_{22}}}. \quad (9)$$

Here, we shall treat a as a phenomenological parameter to be determined experimentally.

For an aligning substrate with easy axis along the unit vector \mathbf{e} , we write the anchoring energy density (per unit area) as

$$W_a := \frac{1}{2}W_0 (1 - (\mathbf{n} \cdot \mathbf{e})^2), \quad (10)$$

where $W_0 > 0$ is the *anchoring strength* [39].

In a $\pi/2$ twist cell bounded by two plates with area A at a distance d , both parallel to the (x, y) plane of a Cartesian frame $(\mathbf{e}_x, \mathbf{e}_y, \mathbf{e}_z)$, we take $\mathbf{e} = \mathbf{e}_x$ for the plate at $z = 0$ and $\mathbf{e} = \mathbf{e}_y$ for the plate at $z = d$ (see Fig. 1). Moreover, we

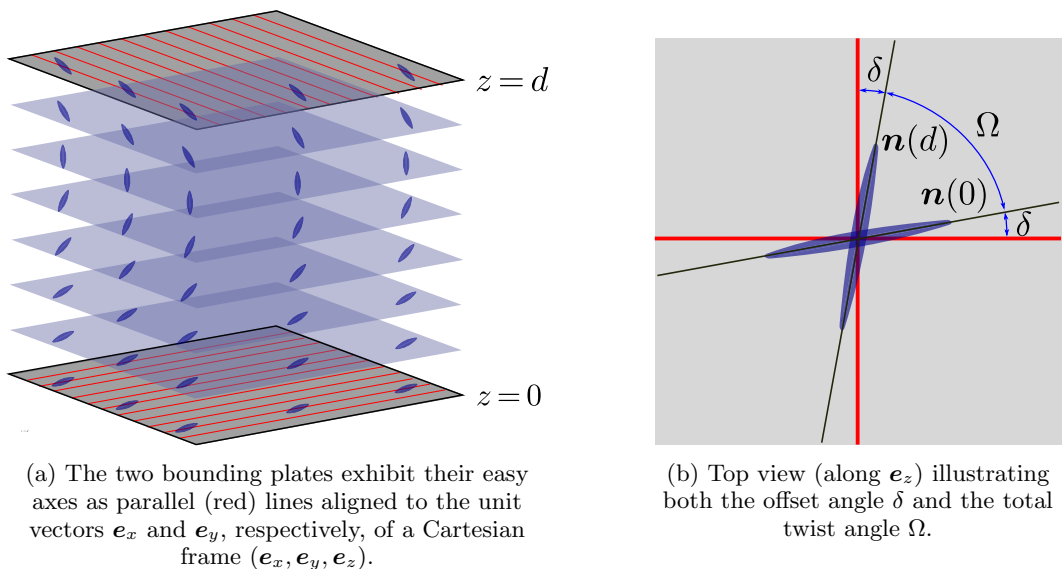


Figure 1: Schematic of a $\pi/2$ twist cell.

assume that the nematic director within the cell is given the form

$$\mathbf{n}(z) = \cos \vartheta(z)\mathbf{e}_x + \sin \vartheta(z)\mathbf{e}_y, \quad (11)$$

where the twist angle ϑ is assumed to be a smooth function of z only. It readily follows from (11) that

$$\nabla \mathbf{n} = \vartheta' (\cos \vartheta \mathbf{e}_y \otimes \mathbf{e}_z - \sin \vartheta \mathbf{e}_x \otimes \mathbf{e}_z), \quad (12)$$

which, also with the aid of (2), implies in turn that

$$S = 0, \quad T = -\vartheta', \quad B = 0, \quad 2q^2 = \frac{1}{2}T^2. \quad (13)$$

By combining (7) and (10), we write the total energy stored in the cell as the functional

$$\mathcal{F}[\vartheta] := \frac{1}{2}A \left\{ \int_0^d K_{22} \left(\vartheta'^2 + \frac{1}{2}a^2 \vartheta'^4 \right) dz - W_0 (\cos^2 \vartheta(0) + \sin^2 \vartheta(d)) \right\}, \quad (14)$$

where a prime $'$ denotes differentiation with respect to z and an inessential additive constant (AW_0) has been omitted. Letting $\zeta := z/d$, we can write \mathcal{F} in the following dimensionless form

$$\mathcal{F}[\vartheta] := \frac{d\mathcal{F}[\vartheta]}{AK_{22}} = \frac{1}{2} \left\{ \int_0^1 \left(\vartheta'^2 + \frac{1}{2}\lambda^2 \vartheta'^4 \right) d\zeta - \alpha (\cos^2 \vartheta(0) + \sin^2 \vartheta(1)) \right\}, \quad (15)$$

where λ and α are dimensionless parameters defined as

$$\lambda := \frac{a}{d}, \quad \text{and} \quad \alpha := \frac{d}{\xi_e}, \quad \text{with} \quad \xi_e := \frac{K_{22}}{W_0}. \quad (16)$$

The parameter α is a relative measure of anchoring strength: the anchoring is *strong* if the *extrapolation* length ξ_e is small compared to d , it is *weak* if ξ_e is large compared with d .

The Euler-Lagrange equations associated with \mathcal{F} is

$$(\vartheta + \lambda^2 \vartheta'^3)' = 0 \quad (17)$$

subject to the boundary conditions

$$(\vartheta' + \lambda^2 \vartheta'^3)|_{\zeta=0} = \frac{1}{2}\alpha \sin 2\vartheta(0), \quad (18a)$$

$$(\vartheta' + \lambda^2 \vartheta'^3)|_{\zeta=1} = \frac{1}{2}\alpha \sin 2\vartheta(1). \quad (18b)$$

Equations (17) and (18) require that there is a constant c such that

$$\vartheta' + \lambda^2 \vartheta'^2 = c \quad (19)$$

and

$$c = \frac{\alpha}{2} \sin 2\vartheta(0) = \frac{\alpha}{2} \sin 2\vartheta(1). \quad (20)$$

It follows from (19) that also ϑ' is constant throughout the cell, and from (20) that there are two classes of equilibrium solutions, characterized by the conditions

$$\vartheta(1) = \vartheta(0) + k\pi, \quad (21a)$$

$$\vartheta(1) = \frac{\pi}{2} - \vartheta(0) + k\pi, \quad (21b)$$

where $k \in \mathbb{Z}$. Since

$$\vartheta' \equiv \vartheta(1) - \vartheta(0), \quad (22)$$

the less distorted (and less energetic) representatives of both classes of solutions (21) are obtained for $k = 0$.

Solution (21a) thus corresponds to the case of *broken* anchoring, for which $c = 0$, $\vartheta \equiv \vartheta_0$, and

$$\mathcal{F}[\vartheta_0] = -\frac{\alpha}{2} \quad \forall \vartheta_0. \quad (23)$$

Letting $\delta := \vartheta(0)$, solution (21b), once combined with (20) and (22), demands that

$$\vartheta' = \frac{\pi}{2} - 2\delta = g_\lambda(\alpha, \delta), \quad (24)$$

where

$$g_\lambda(\alpha, \delta) := \frac{1}{\lambda} \frac{6^{2/3} \left(\sqrt{(9\alpha\lambda \sin 2\delta)^2 + 48} + 9\alpha\lambda \sin 2\delta \right)^{2/3} - 12}{6^{4/3} \left(\sqrt{(9\alpha\lambda \sin 2\delta)^2 + 48} + 9\alpha\lambda \sin 2\delta \right)^{1/3}} \quad (25)$$

is the real root of the cubic equation

$$g(1 + \lambda^2 g^2) = \frac{\alpha}{2} \sin 2\delta. \quad (26)$$

It is shown in Appendix A that the total energy associated with the latter equilibrium solution is always less than $\mathcal{F}[\vartheta_0]$ in (23), so that the anchoring is never broken.

Figure 2 illustrates the graphical solution of (24): there is only one intersection between the graph of g_λ and the

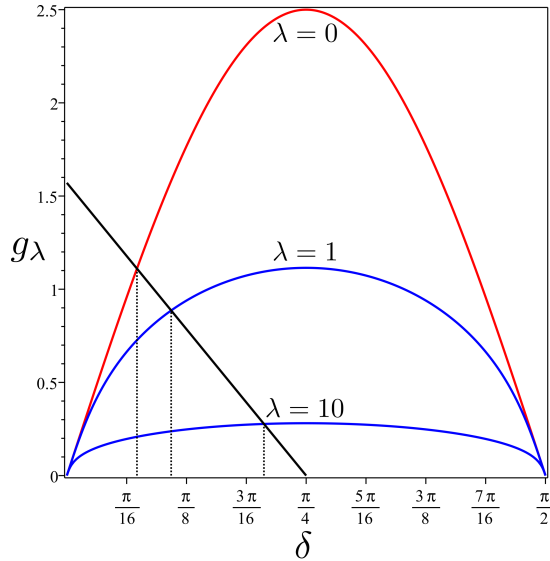


Figure 2: Graphical solution of (24). The graph of $g_\lambda(\alpha, \delta)$ against δ is drawn for $\alpha = 5$ and several values of λ . For $\lambda = 0$, the red curve represents the graph of g_0 in (27). The black straight line is the graph of $\frac{\alpha}{2} - 2\delta$, which has a single intersection with the graph of each g_λ .

straight line $\frac{\alpha}{2} - 2\delta$; it falls for $\delta = \delta_0(\alpha, \lambda)$. Figure 3 shows how δ_0 depends on both λ and α . In the limit as λ tends to 0, we retrieve the quadratic case already studied in [10] and [15], for which (25) reduces to

$$g_0(\alpha, \delta) := \frac{\alpha}{2} \sin 2\delta. \quad (27)$$

For α small, $\delta_0(\alpha, \lambda)$ approaches $\frac{\pi}{4}$ for all values of λ . When α increases, $\delta_0(\alpha, \lambda)$ is an increasing function of λ that exhibits a larger excursion as α increases. For any given value of λ , $\delta_0(\alpha, \lambda)$ tends to $\frac{\pi}{4}$ as α tends to 0 and decreases monotonically as α increases, with an excursion that grows larger as λ decreases (see Fig. 3). The total equilibrium twist angle is then given as a function of (α, λ) by

$$\Omega(\alpha, \lambda) = \frac{\pi}{2} - 2\delta_0(\alpha, \lambda). \quad (28)$$

We shall see in the following section how Ω has effectively been measured by optical means in [10] and [15]. We shall fit their data to determine both α and λ (that is, both W_0 and a , once K_{22} is obtained from independent measurements).

III. EXPERIMENTS REINTERPRETATION

Here, we reexamine the experiments performed in [10] and [15].

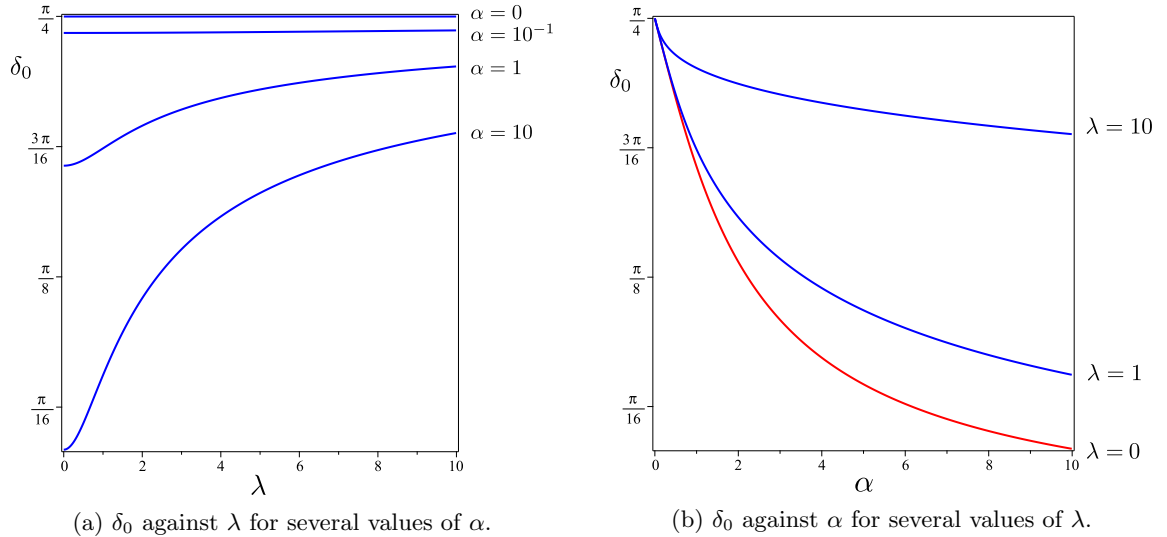


Figure 3: Plots showing how the root δ_0 of (24) depends on both λ and α

In [10], an aqueous solution of disodium cromoglycate (DSCG) (at a concentration 16.0% (wt/wt) and temperature 25°C) was used to fill a $\pi/2$ twist cell bounded by plates with different rubbed PI aligning substrates. Linearly polarized monochromatic light was shone perpendicularly on one plate of the cell and detected on the other plate through a linear polarizer aligned in a direction either orthogonal or parallel to the polarization of the incoming light. The cell was rotated around the direction of light propagation and the transmitted intensity $I(\theta)$ (scaled to the intensity of the incoming light) was monitored as a function of the rotation angle θ .

A theory put forward by McIntyre [40, 41] related (in closed form) the total twist angle Ω to both the minimum and maximum values of $I(\theta)$, I_{\perp}^{\min} and I_{\perp}^{\max} , respectively, when the polarizers at the bounding plates are orthogonal to one another. Following [42] and [19] (see also p. 174 of [43]), we give these scaled intensities the following expressions,

$$I_{\perp}^{\min}(\Omega) = \left(\cos \tau \sin \Omega - \frac{\Omega}{\tau} \sin \tau \cos \Omega \right)^2, \quad (29a)$$

$$I_{\perp}^{\max}(\Omega) = \left(1 - \frac{\Omega^2}{\tau^2} \right) \sin^2 \tau + \left(\cos \tau \sin \Omega - \frac{\Omega}{\tau} \sin \tau \cos \Omega \right)^2, \quad (29b)$$

where $\tau := \sqrt{4\Omega^2 + \Psi^2}/2$ and $\Psi := (2\pi/\lambda_0)d\Delta n$ is the phase retardation angle; here λ_0 is the wavelength of the light in vacuum and Δn is the birefringence of the material.⁴ Similarly, the minimum and maximum (scaled) intensities, I_{\parallel}^{\min} and I_{\parallel}^{\max} , transmitted through parallel polarizers are given by

$$I_{\parallel}^{\min}(\Omega) = 1 - I_{\perp}^{\max}(\Omega), \quad (29c)$$

$$I_{\parallel}^{\max}(\Omega) = 1 - I_{\perp}^{\min}(\Omega). \quad (29d)$$

All intensities in (29) are very sensitive to Ω [19]. On the other hand, as pointed out in [10], both these and the *intensity ratio*

$$R(\Omega) := \frac{I_{\perp}^{\max}(\Omega) - I_{\parallel}^{\min}(\Omega)}{I_{\perp}^{\max}(\Omega) + I_{\parallel}^{\min}(\Omega)} = 2I_{\perp}^{\max}(\Omega) - 1, \quad (30)$$

which ranges in the interval $[-1, 1]$, are rather insensitive to the incident light intensity.

⁴ Equation (29a) is equivalent to equation (1) of [15], provided in the latter one corrects the typo that made appear $(X \sin \tau / \sqrt{1 + X^2})^2$ as $(\sin \tau / \sqrt{1 + X^2})^2$. Moreover, a perfectly equivalent form of (29b) would be the following,

$$I_{\perp}^{\max}(\Omega) = \left(1 - \frac{\Omega^2}{\tau^2} \right) \sin^2 \Omega + \left(\cos \Omega \sin \tau - \frac{\Omega}{\tau} \sin \Omega \cos \tau \right)^2.$$

In [10], R was measured at different values of the thickness d in a wedge cell with rubbed SE-7511L PI substrates for $\lambda_0 = 633$ nm and $\Delta n = -0.0184$ (measured in [10] for DSCG at concentration 16.0%(wt/wt) and temperature 25°C).

The data taken from Fig. 4 of [10] are represented by dots in Fig.4 below; they can be fitted to the theoretical functions in (30) and (29b), with the total twist angle Ω given by (28), for both $\lambda = 0$ and $\lambda > 0$. The former case

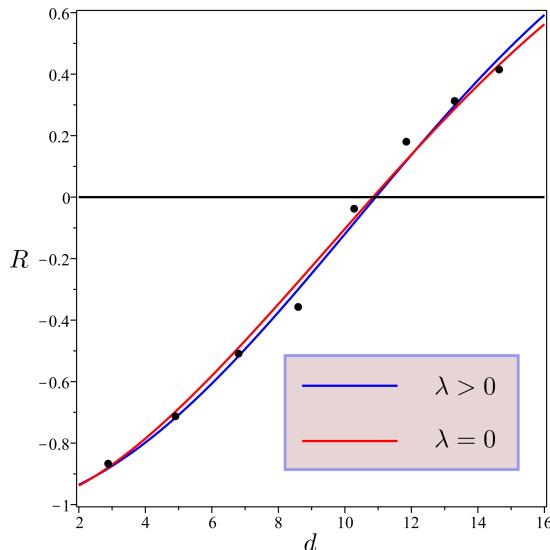


Figure 4: Best fits of the data for the intensity ratio R in Fig. 4 of [10] with the theoretical functions given by (30) and (29b) when the total twist angle Ω is delivered by (28). Red curve (classical quadratic theory): $\lambda = 0$ and α is the only fitting parameter. Blue curve (quartic twist theory): $\lambda > 0$ is set free and used as a fitting parameter alongside with α . The quartic twist theory is apparently more successful than the quadratic theory. Quantitative estimates of the error are given for both curves in Appendix B.

($\lambda = 0$) corresponds to the classical quadratic theory and was already considered in [10]: the only fitting parameter is α , and for $K_{22} \approx 0.7$ pN (value obtained from [44] for DSCG at concentration 16.0% (wt/wt) and temperature 25°C) the best fit delivers $W_0 \approx 0.37 \mu\text{J}/\text{m}^2$, in complete agreement with [10]. Alternatively, we can set λ free and seek the best fit of the data by adjusting both α and $\lambda > 0$: the best fit then delivers

$$a \approx 1 \mu\text{m}, \quad W_0 \approx 1.55 \mu\text{J}/\text{m}^2. \quad (31)$$

Fig. 4 represents the results of both fits. It suggests that the quartic twist theory ($\lambda > 0$) fits better the data than the classical quadratic theory ($\lambda = 0$). This is confirmed quantitatively by the error estimate presented in Appendix B.

A similar experiment was conducted in [15] to measure W_0 for photoinduced planar anchoring of DSCG at concentration 14.0%(wt/wt) and temperature 25°C (substrates were coated with dye SD1 separated from the LCLC by a layer of RM257).

The scaled light intensities I_{\perp}^{\min} and I_{\perp}^{\max} were measured for different values of the thickness d in a wedge cell for $\lambda_0 = 633$ nm and $\Delta n = -0.018$. By using Ω as fitting parameter to best reproduce the experimental data via the theoretical functions in (29a) and (29b), in [15] the classical quadratic theory enabled to estimate $W_0 = 1.7 \pm 0.2 \mu\text{J}/\text{m}^2$.

The experimental data taken from Fig. 2 of [15] are represented in Fig.5. Here, with the aid of (29a) and (29b), they will be processed by the same fitting strategy applied above to the other experiment, for both $\lambda = 0$ and $\lambda > 0$. In the former case, the only fitting parameter is α , and for $K_{22} \approx 0.5$ pN (value obtained from [44] for DSCG at concentration 14.0% (wt/wt) and temperature 25°C) the best fit delivers $W_0 \approx 1.51 \mu\text{J}/\text{m}^2$, which falls within the error bar of the measurement of [15]. The general best fit that utilizes both α and $\lambda > 0$ as adjusting parameters delivers

$$a \approx 4.8 \mu\text{m}, \quad W_0 \approx 1.65 \mu\text{J}/\text{m}^2. \quad (32)$$

Fig. 5 represents the results of both fits: once again, the quartic twist theory ($\lambda > 0$) improves over the classical quadratic theory ($\lambda = 0$). (Further quantitative details are presented in Appendix B.)

We finally comment on the difference (mainly in a) between the estimates in (31) and (32). As shown in (30), the data for the intensity ratio R fitted in Fig. 4 ultimately contain only the data for the scaled intensity I_{\perp}^{\max} , whereas the data for both I_{\perp}^{\max} and I_{\perp}^{\min} are jointly fitted in Fig. 5. This inclines us to consider the estimate in (32) more reliable than the estimate in (31).

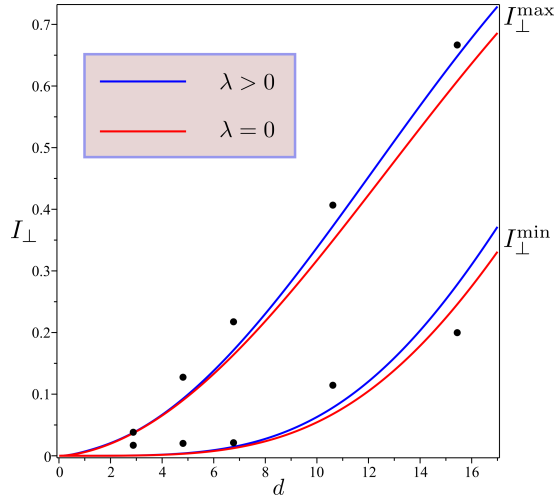


Figure 5: Best combined fits of the data for the scaled light intensities I_{\perp}^{\min} and I_{\perp}^{\max} in Fig. 2 of [15] with the theoretical functions given by (29a) and (29b) when the total twist angle Ω is delivered by (28). Red curves (classical quadratic theory): $\lambda = 0$ and α is the only fitting parameter. Blue curves (quartic twist theory): $\lambda > 0$ is set free and used as a fitting parameter alongside with α . Again, the quartic twist theory is more successful than the quadratic theory; further quantitative details are given in Appendix B.

IV. CONCLUSION

A quartic twist theory for chromonic liquid crystals is applied to a $\pi/2$ twist cell. Like the classical quadratic theory, it predicts a linear twist within the cell, with a total twist angle related to both the anchoring strength W_0 at the bounding substrates and a new phenomenological length a .

Reinterpreting two recent experiments, we showed that the quartic twist theory affords a better representation of the data compared to the classical quadratic theory and estimates an anchoring strength W_0 approximately four times larger in one case, and nearly equal in the other. The phenomenological length a estimated here for DSCG turned out to be closer to the value estimated in [29] for SSY ($a \approx 6.4 \mu\text{m}$) than to that estimated in [32] for SSY (a ranging from $33 \mu\text{m}$ to $54 \mu\text{m}$ in different physical conditions). Such a wide range of values for a is not yet understood, as we still lack a microscopic model to describe the origin and nature of this phenomenological parameter.

We are aware that a systematic collection of data would be required to achieve a sound experimental determination of both W_0 and a for different materials and varying concentration and temperature. We hope that such an endeavour could be undertaken in the future; this paper has only shown what is perhaps one way to go.

Appendix A: Energy Comparison

To make sure that the anchoring at the cell's plates is never broken, no matter how small W_0 is, we need compare the minimum total energy \mathcal{F} computed on the linear twist solving (24), with the energy of the broken anchoring in (23).

To this end, we first note that by (24) the minimum of \mathcal{F} can easily be expressed as a function F of δ_0 ,

$$F(\delta_0) := \frac{1}{2} \left(\frac{\pi}{2} - 2\delta_0 \right)^2 \left[1 + \frac{\lambda^2}{2} \left(\frac{\pi}{2} - 2\delta_0 \right)^2 \right] - \alpha \cos^2 \delta_0. \quad (\text{A1})$$

Since δ_0 is determined numerically, and so we lack its explicit expression in terms of α and λ , we replace it with a test function δ_{test} that reproduces the same behaviour as δ_0 for $\alpha \rightarrow 0$, $\alpha \rightarrow \infty$, and $\lambda \rightarrow \infty$, and is chosen so that

$$\Delta F_{\text{test}} := F(\delta_{\text{test}}) - \mathcal{F}[\vartheta_0] = F(\delta_{\text{test}}) + \frac{\alpha}{2} < 0, \quad (\text{A2})$$

where use has been made of (23). This would suffice to prove that $F(\delta_0) < \mathcal{F}[\vartheta_0]$, as $F(\delta_0) \leq F(\delta_{\text{test}})$, being $F(\delta_0)$ the minimum of \mathcal{F} .

We took

$$\delta_{\text{test}} := \frac{\pi}{2 \left(\frac{\alpha}{1+\lambda^2} + 2 \right)}, \quad (\text{A3})$$

which, once inserted in (A2), led us to show with little labour that, for any given $\lambda > 0$, ΔF_{test} is a decreasing function of α , whose derivative vanishes only for $\alpha = 0$, which possesses the following asymptotic behaviours,

$$\Delta F_{\text{test}} = -\frac{\pi}{8(1+\lambda^2)} \left[1 - \frac{\pi}{8(1+\lambda^2)} \right] \alpha^2 + \mathcal{O}(\alpha^3), \quad (\text{A4})$$

$$\Delta F_{\text{test}} = -\frac{\alpha}{2} + \mathcal{O}\left(\frac{1}{\alpha}\right), \quad (\text{A5})$$

for $\alpha \rightarrow 0$ and $\alpha \rightarrow \infty$, respectively. This indeed proves our claim (A2).

Appendix B: Error Estimates

Here we describe in some detail the strategy adopted to fit the data shown in Figs. 4 and 5 of the main text. First, we introduce a dimensionless parameter, λ^* , which is independent of the cell's thickness d ,

$$\lambda^* := \alpha\lambda = \frac{aW_0}{K_{22}}. \quad (\text{B1})$$

Then, with the aid of (28), we rewrite (24) as an equation for Ω in the parameters (λ, λ^*) ,

$$\Omega = \frac{1}{\lambda} \frac{6^{2/3} \left(\sqrt{(9\lambda^* \cos \Omega)^2 + 48} + 9\lambda^* \cos \Omega \right)^{2/3} - 12}{6^{4/3} \left(\sqrt{(9\lambda^* \cos \Omega)^2 + 48} + 9\lambda^* \cos \Omega \right)^{1/3}}. \quad (\text{B2})$$

In the experiment performed in [10], eight values d_i ($i = 1, \dots, 8$) of the thickness d were selected, ranging from $d_1 \approx 2.9 \mu\text{m}$ to $d_8 \approx 14.7 \mu\text{m}$, and the corresponding values R_i of the intensity ratio R were then measured. We set

$$\lambda_1 := \frac{a}{d_1} \quad (\text{B3})$$

and regard this as a fitting parameter. Clearly, letting $\lambda_i := a/d_i$, all these parameters are determined by λ_1 and the measured d_i 's,

$$\lambda_i = \lambda_1 \frac{d_1}{d_i}. \quad (\text{B4})$$

For given λ_1 and λ^* , we denote $\Omega_i(\lambda_1, \lambda^*)$ the root of (B2) with $\lambda = \lambda_i$ and compute the error

$$\mathbf{E}(\lambda_1, \lambda^*) := \frac{\sum_{i=1}^8 [R(\Omega_i(\lambda_1, \lambda^*)) - R_i]^2}{8}, \quad (\text{B5})$$

where $R(\Omega)$ is the function in (30). The function \mathbf{E} has been studied numerically and found to have a single minimum in λ_1 , for every given value of $\lambda^* > 0$; the path of these constrained minima, parametrized in λ^* , is shown in Fig. 6. The absolute minimum of $\mathbf{E} \approx 13.48 \times 10^{-4}$ is attained at

$$\lambda_1 \doteq 0.344, \quad \lambda^* \doteq 2.01. \quad (\text{B6})$$

For $K_{22} \approx 0.7 \text{pN}$ and $d_1 \approx 2.9 \mu\text{m}$, from (B6) we estimate the optimal values for a and W_0 in (31).

The graph of the curve that represents R in Fig. 4 was obtained by plotting the function in (30) for Ω given in terms of d by the root of (B2) for λ^* as in (B6) and $\lambda = a/d$, where a is the optimal value in (31).

For $\lambda = 0$, the error estimate goes along slightly different lines. By (27) and (28), (B2) is now replaced by

$$\Omega = \frac{\alpha}{2} \cos \Omega. \quad (\text{B7})$$

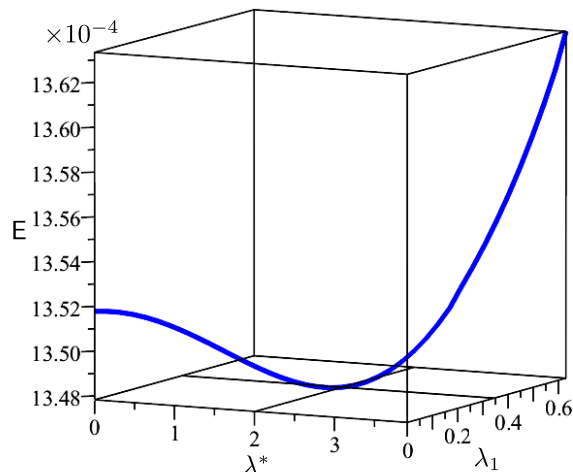


Figure 6: Three-dimensional graph illustrating the path $\lambda^* \mapsto \min_{\lambda_1} E(\lambda_1, \lambda^*)$. In the limit as $\lambda^* \rightarrow 0$, the minimum of E in λ_1 is attained at $\lambda_1 = 0$; its value equals the minimum of E_0 in (B9).

We denote by $\Omega_i(\xi_1)$ the root of (B7) for α given by

$$\alpha_i = \frac{1}{\xi_1} \frac{d_i}{d_1}, \quad (\text{B8})$$

where $\xi_1 := \xi_e/d_1$. The latter is treated as a fitting parameter featuring in the error

$$E_0(\xi_1) := \frac{\sum_{i=1}^8 [R(\Omega_i(\xi_1)) - R_i]^2}{8}. \quad (\text{B9})$$

The minimum of E_0 was found for $\xi_1 \doteq 0.655$, which for $K_{22} \approx 0.7$ pN corresponds to $\xi_e \approx 1.9 \mu\text{m}$ and $W_0 \approx 0.37 \mu\text{J}/\text{m}^2$, in complete agreement with [10]. The minimum of E_0 is approximately 13.52×10^{-4} , which equals the minimum of E in (B5) for $\lambda_1 = 0$ (see Fig. 6). Thus, the quartic theory affords an error that is estimated to be 3% less than the error of the quadratic theory. This proves that the data shown in Fig. 4 are indeed better approximated for $\lambda > 0$. The red curve that represents R in Fig. 4 was obtained by plotting the function in (30) for Ω given in terms of d by the root of (B7) for $\alpha = d/\xi_e$, where ξ_e is the optimal value just determined.

Similarly, in the experiment performed in [15], five values d_i ($i = 1, \dots, 5$) of the thickness d were selected, ranging from $d_1 \approx 2.9 \mu\text{m}$ to $d_5 \approx 15.5 \mu\text{m}$, and the corresponding values of minimum and maximum relative intensities, $I_{\perp,i}^{\min}$ and $I_{\perp,i}^{\max}$, were measured. The error E is now more appropriately defined as

$$E(\lambda_1, \lambda^*) := \frac{\sum_{i=1}^5 \left(\left[I_{\perp}^{\max}(\Omega_i(\lambda_1, \lambda^*)) - I_{\perp,i}^{\max} \right]^2 + \left[I_{\perp}^{\min}(\Omega_i(\lambda_1, \lambda^*)) - I_{\perp,i}^{\min} \right]^2 \right)}{10}. \quad (\text{B10})$$

The minimum in λ_1 of E for given λ^* is shown in Fig. 7. The absolute minimum of $E \approx 14.32 \times 10^{-4}$ is attained at

$$\lambda_1 \doteq 1.67, \quad \lambda^* \doteq 16. \quad (\text{B11})$$

For $K_{22} \approx 0.5$ pN and $d_1 \approx 2.9 \mu\text{m}$, from (B11) we estimate the optimal values for a and W_0 in (32). The graphs of the blue curves in Fig. 5 were obtained precisely as that in Fig. 4.

For $\lambda = 0$, the error is given by

$$E_0(\xi_1) := \frac{\sum_{i=1}^5 \left(\left[I_{\perp}^{\max}(\Omega_i(\xi_1)) - I_{\perp,i}^{\max} \right]^2 + \left[I_{\perp}^{\min}(\Omega_i(\xi_1)) - I_{\perp,i}^{\min} \right]^2 \right)}{10}. \quad (\text{B12})$$

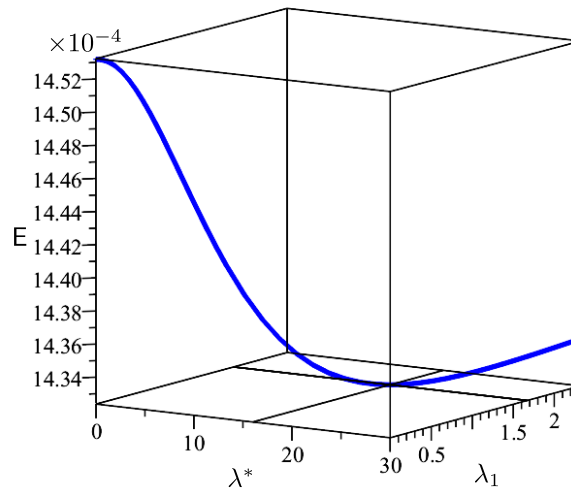


Figure 7: Three-dimensional graph illustrating the path $\lambda^* \mapsto \min_{\lambda_1} E(\lambda_1, \lambda^*)$, very similar to the one in Fig. 6.

The minimum of $E_0 \approx 14.53 \times 10^{-4}$ was found for $\xi_1 \doteq 0.11$, which for $K_{22} \approx 0.5$ pN corresponds to $\xi_e \approx 0.33 \mu\text{m}$ and $W_0 \approx 1.51 \mu\text{J}/\text{m}^2$. Thus, the error of the quartic theory is 1.4% less than the error of the quadratic one. Finally, also the red curves in Fig. 5 were obtained precisely as that in Fig. 4.

ACKNOWLEDGMENTS

We are grateful to an anonymous Reviewer of an earlier version of this paper for their suggestions, which have improved our work.

-
- [1] Lydon J. Chromonic liquid crystal phases. *Curr Opin Colloid Interface Sci.* 1998;3(5):458–466. Available from: <https://www.sciencedirect.com/science/article/pii/S1359029498800198>.
 - [2] Lydon J. Chromonics. In: Demus D, Goodby J, Gray GW, Spiess HW, Vill V, editors. *Handbook of Liquid Crystals: Low Molecular Weight Liquid Crystals II*. Weinheim, Germany: John Wiley & Sons; 1998. p. 981–1007.
 - [3] Lydon J. Chromonic review. *J Mater Chem.* 2010;20:10071–10099. Available from: <http://dx.doi.org/10.1039/B926374H>.
 - [4] Lydon J. Chromonic liquid crystalline phases. *Liq Cryst.* 2011;38(11–12):1663–1681. Available from: <https://doi.org/10.1080/02678292.2011.614720>.
 - [5] Dierking I, Martins Figueiredo Neto A. Novel Trends in Lyotropic Liquid Crystals. *Crystals.* 2020;10(7):604. Available from: <https://www.mdpi.com/2073-4352/10/7/604>.
 - [6] Shiyanovskii SV, Schneider T, Smalyukh II, Ishikawa T, Niehaus GD, Doane KJ, et al. Real-time microbe detection based on director distortions around growing immune complexes in lyotropic chromonic liquid crystals. *Phys Rev E.* 2005;71:020702. Available from: <https://link.aps.org/doi/10.1103/PhysRevE.71.020702>.
 - [7] Mushenheim PC, Trivedi RR, Tuson HH, Weibel DB, Abbott NL. Dynamic self-assembly of motile bacteria in liquid crystals. *Soft Matter.* 2014;10:88–95. Available from: <http://dx.doi.org/10.1039/C3SM52423J>.
 - [8] Mushenheim PC, Trivedi RR, Weibel D, Abbott N. Using liquid crystals to reveal how mechanical anisotropy changes interfacial behaviors of motile bacteria. *Biophys J.* 2014;107 1:255–265. Available from: <https://www.sciencedirect.com/science/article/pii/S0006349514004664>.
 - [9] Zhou S, Sokolov A, Lavrentovich OD, Aranson IS. Living liquid crystals. *Proc Natl Acad Sci USA.* 2014;111(4):1265–1270. Available from: <https://www.pnas.org/doi/10.1073/pnas.1321926111>.
 - [10] Collings PJ, van der Asdonk P, Martinez A, Tortora L, Kouwer PHJ. Anchoring strength measurements of a lyotropic

- chromonic liquid crystal on rubbed polyimide surfaces. *Liq Cryst.* 2017;44(7):1165–1172. Available from: <https://doi.org/10.1080/02678292.2016.1269372>.
- [11] Yip WC, Kwok HS, Kozenkov VM, Chigrinov VG. Photo-patterned E-wave polarizer. *Displays.* 2001;22(1):27–32. Available from: <https://www.sciencedirect.com/science/article/pii/S0141938201000518>.
- [12] Ichimura K, Fujiwara T, Momose M, Matsunaga D. Surface-assisted photoalignment control of lyotropic liquid crystals. Part 1. Characterisation and photoalignment of aqueous solutions of a water-soluble dye as lyotropic liquid crystals. *J Mater Chem.* 2002;12:3380–3386. Available from: <http://dx.doi.org/10.1039/B208310H>.
- [13] Fujiwara T, Ichimura K. Surface-assisted photoalignment control of lyotropic liquid crystals. Part 2. Photopatterning of aqueous solutions of a water-soluble anti-asthmatic drug as lyotropic liquid crystals. *J Mater Chem.* 2002;12:3387–3391. Available from: <http://dx.doi.org/10.1039/B208311F>.
- [14] van der Asdonk P, Hendrikse HC, Fernandez-Castano Romera M, Voerman D, Ramakers BEI, Löwik DWPM, et al. Patterning of Soft Matter across Multiple Length Scales. *Adv Func Mater.* 2016;26(16):2609–2616. Available from: <https://onlinelibrary.wiley.com/doi/abs/10.1002/adfm.201504945>.
- [15] Peng C, Guo Y, Turiv T, Jiang M, Wei QH, Lavrentovich OD. Patterning of Lyotropic Chromonic Liquid Crystals by Photoalignment with Photonic Metamasks. *Adv Mater.* 2017;29(21):1606112. Available from: <https://onlinelibrary.wiley.com/doi/abs/10.1002/adma.201606112>.
- [16] Nastishin YA, Liu H, Schneider T, Nazarenko V, Vasyuta R, Shiyanovskii SV, et al. Optical characterization of the nematic lyotropic chromonic liquid crystals: Light absorption, birefringence, and scalar order parameter. *Phys Rev E.* 2005;72:041711. Available from: <https://link.aps.org/doi/10.1103/PhysRevE.72.041711>.
- [17] Tone CM, De Santo MP, Buonomenna MG, Golemme G, Ciuchi F. Dynamical homeotropic and planar alignments of chromonic liquid crystals. *Soft Matter.* 2012;8:8478–8482. Available from: <http://dx.doi.org/10.1039/C2SM26021B>.
- [18] Zhou S, Nastishin YA, Omelchenko MM, Tortora L, Nazarenko VG, Boiko OP, et al. Elasticity of Lyotropic Chromonic Liquid Crystals Probed by Director Reorientation in a Magnetic Field. *Phys Rev Lett.* 2012;109:037801. Available from: <https://link.aps.org/doi/10.1103/PhysRevLett.109.037801>.
- [19] McGinn CK, Laderman LI, Zimmermann N, Kitzerow HS, Collings PJ. Planar anchoring strength and pitch measurements in achiral and chiral chromonic liquid crystals using 90-degree twist cells. *Phys Rev E.* 2013;88:062513. Available from: <https://link.aps.org/doi/10.1103/PhysRevE.88.062513>.
- [20] Yi Y, Clark NA. Orientation of chromonic liquid crystals by topographic linear channels: multi-stable alignment and tactoid structure. *Liq Cryst.* 2013;40(12):1736–1747. Available from: <https://doi.org/10.1080/02678292.2013.839831>.
- [21] Kim JY, Nayani K, Jeong HS, Jeon HJ, Yoo HW, Lee EH, et al. Macroscopic alignment of chromonic liquid crystals using patterned substrates. *Phys Chem Chem Phys.* 2016;18:10362–10366. Available from: <http://dx.doi.org/10.1039/C5CP07570J>.
- [22] Ericksen JL. Inequalities in Liquid Crystal Theory. *Phys Fluids.* 1966;9(6):1205–1207. Available from: <https://doi.org/10.1063/1.1761821>.
- [23] Papparini S, Virga EG. Paradoxes for chromonic liquid crystal droplets. *Phys Rev E.* 2022;106:044703. Available from: <https://link.aps.org/doi/10.1103/PhysRevE.106.044703>.
- [24] Tortora L, Park HS, Kang SW, Savaryn V, Hong SH, Kaznatcheev K, et al. Self-assembly, condensation, and order in aqueous lyotropic chromonic liquid crystals crowded with additives. *Soft Matter.* 2010;6:4157–4167. Available from: <http://dx.doi.org/10.1039/C0SM00065E>.
- [25] Tortora L, Lavrentovich OD. Chiral symmetry breaking by spatial confinement in tactoidal droplets of lyotropic chromonic liquid crystals. *Proc Natl Acad Sci USA.* 2011;108(13):5163–5168. Available from: <https://doi.org/10.1073/pnas.1100087108>.
- [26] Peng C, Lavrentovich OD. Chirality Amplification and Detection by Tactoids of Lyotropic Chromonic Liquid Crystals. *Soft Matter.* 2015;11:7221–7446. Available from: <http://dx.doi.org/10.1039/C5SM01632K>.
- [27] Nayani K, Fu J, Chang R, Park JO, Srinivasarao M. Using chiral tactoids as optical probes to study the aggregation behavior of chromonics. *Proc Natl Acad Sci USA.* 2017;114(15):3826–3831. Available from: <https://www.pnas.org/doi/full/10.1073/pnas.1614620114>.
- [28] Shadpour S, Vanegas JP, Nemati A, Hegmann T. Amplification of Chirality by Adenosine Monophosphate-Capped Luminescent Gold Nanoclusters in Nematic Lyotropic Chromonic Liquid Crystal Tactoids. *ACS Omega.* 2019;4:1662–1668. Available from: <https://doi.org/10.1021/acsomega.8b03335>.
- [29] Papparini S, Virga EG. An Elastic Quartic Twist Theory for Chromonic Liquid Crystals. *J Elast.* 2023; Available from: <https://doi.org/10.1007/s10659-022-09983-4>.
- [30] Papparini S, Virga EG. Spiralling defect cores in chromonic hedgehogs. *Liq Cryst.* 2023;50(7–10):1498–1516. Available from: <https://doi.org/10.1080/02678292.2023.2190626>.
- [31] Spina L, De Santo MP, Tone CM, Pisani M, Vita F, Barberi R, et al. Intercalation or external binding: How to torque chromonic Sunset Yellow. *J Mol Liq.* 2022;359:119265. Available from: <https://www.sciencedirect.com/science/article/pii/S0167732222008030>.
- [32] Ciuchi F, De Santo MP, Papparini S, Spina L, Virga EG. Inversion ring in chromonic twisted hedgehogs: theory and experiment. *Liquid Crystals.* 2024; Available from: <https://doi.org/10.1080/02678292.2024.2313023>.
- [33] Selinger JV. Interpretation of saddle-splay and the Oseen-Frank free energy in liquid crystals. *Liq Cryst Rev.* 2018;6:129–142. Available from: <https://doi.org/10.1080/21680396.2019.1581103>.
- [34] Pedrini A, Virga EG. Liquid crystal distortions revealed by an octupolar tensor. *Phys Rev E.* 2020;101:012703. Available from: <https://link.aps.org/doi/10.1103/PhysRevE.101.012703>.
- [35] Selinger JV. Director Deformations, Geometric Frustration, and Modulated Phases in Liquid Crystals. *Ann Rev Condens*

- Matter Phys. 2022;13:49–71. Available from: <https://doi.org/10.1146/annurev-conmatphys-031620-105712>.
- [36] Long C, Selinger JV. Explicit demonstration of geometric frustration in chiral liquid crystals. *Soft Matter*. 2023;19:519–529. Available from: <http://dx.doi.org/10.1039/D2SM01420C>.
- [37] Virga EG. Uniform distortions and generalized elasticity of liquid crystals. *Phys Rev E*. 2019;100:052701. Available from: <https://link.aps.org/doi/10.1103/PhysRevE.100.052701>.
- [38] Papani S, Virga EG. Stability Against the Odds: the Case of Chromonic Liquid Crystals. *J Nonlinear Sci*. 2022;32:74. Available from: <https://doi.org/10.1007/s00332-022-09833-6>.
- [39] Rapini A, Papoular M. Distorsion d'une lamelle nématique sous champ magnétique conditions d'ancrage aux parois. *J Phys Colloq*. 1969;30(C4):C4.54–C4.56. Available from: <https://hal.archives-ouvertes.fr/jpa-00213715/document>.
- [40] McIntyre P, Snyder AW. Light propagation in twisted anisotropic media: Application to photoreceptors. *J Opt Soc Am*. 1978;68(2):149–157. Available from: <https://opg.optica.org/abstract.cfm?URI=josa-68-2-149>.
- [41] McIntyre P. Transmission of light through a twisted nematic liquid-crystal layer. *J Opt Soc Am*. 1978;68(6):869–872. Available from: <https://opg.optica.org/abstract.cfm?URI=josa-68-6-869>.
- [42] Ong HL. Origin and characteristics of the optical properties of general twisted nematic liquid-crystal displays. *J Appl Phys*. 1988 07;64(2):614–628. Available from: <https://doi.org/10.1063/1.341951>.
- [43] Khoo IC. *Liquid Crystals*. 2nd ed. Hoboken, New Jersey, USA: John Wiley & Sons; 2007.
- [44] Zhou S, Neupane K, Nastishin YA, Baldwin AR, Shiyanovskii SV, Lavrentovich OD, et al. Elasticity, viscosity, and orientational fluctuations of a lyotropic chromonic nematic liquid crystal disodium cromoglycate. *Soft Matter*. 2014;10:6571–6581. Available from: <http://dx.doi.org/10.1039/C4SM00772G>.